Computers and Electronics in Agriculture 185 (2021) 106118

Contents lists available at ScienceDirect

Computers and Electronics in Agriculture

journal homepage: www.elsevier.com/locate/compag

Original papers

Sentinel-1 interferometric coherence and backscattering analysis for crop monitoring

Rouhollah Nasirzadehdizaji [a,*], Ziyadin Cakir [b], Fusun Balik Sanli [a], Saygin Abdikan [c], Antonio Pepe [d], Fabiana Calò [d]

[a] Department of Geomatic Engineering, Yildiz Technical University, 34220 Istanbul, Turkey
[b] Department of Geological Engineering, Faculty of Mines, Istanbul Technical University, 34469 Istanbul, Turkey
[c] Geomatics Engineering Department, Hacettepe University, 06800 Ankara, Turkey
[d] Institute for Electromagnetic Sensing of the Environment (IREA), Italian National Research Council, 328 Diocleziano, 80124 Napoli, Italy

ARTICLE INFO

Keywords:
Multitemporal Sentinel-1
InSAR
Coherence
SAR intensities
Agriculture

ABSTRACT

In this study, we investigate the synergic use of synthetic aperture radar (SAR) backscattering (i.e., sigma nought σ^0) and InSAR coherence (γ) maps as a tool for crop growth monitoring. Experiments were carried out using Sentinel-1 TOPS SAR data and field observations in one of the State General Directorate of Agriculture Enterprise farms in Konya (Central Turkey). The phenological stages of maize, sunflower, and wheat have been analyzed and compared to coherence and backscatter time series of Sentinel-1 data on multiple tracks and polarizations. The results evidence a strong correlation between different phenological stages of the crops and the InSAR coherence. Specifically, the observed coherence values are the highest for the maize ($\gamma_{asc,\ desc} = 0.47$) and sunflower ($\gamma_{asc} = 0.49$, $\gamma_{desc} = 0.48$) after plowing the fields and seeding the crops. The coherence decreases with the plants' growth and reaches the lowest values for maize, sunflower, and wheat ($\gamma = 0.08$, $\gamma = 0.09$ and $\gamma = 0.07$, respectively) when the ground is completely covered by plants. Then, a coherence increase is observed after the harvesting time ($\gamma = 0.51$, $\gamma = 0.50$ and $\gamma = 0.42$ for maize, sunflower, and wheat, respectively). In terms of multi-temporal SAR backscattering, we find significant changes of the σ^0 values during the crops' growing stages due to the changes in their leaf geometry and physical structure. The highest σ^0 values for the maize, sunflower, and wheat are obtained as −9.18 dB, −5.24 dB and −10.05 dB, respectively, for the ascending orbit, in mid growing stages. Results show the improved capacity of SAR-driven measurements for agriculture monitoring and precise farming activities when InSAR coherence and backscattering are synergistically used. Specifically, the coherence allows estimating the main growth stages of the different crop types. Moreover, SAR backscattering provides reliable information on the whole growth stages during the agricultural season, and it might be profitably exploited for crop assessment.

1. Introduction

Crops as food resources have a substantial importance for the sustainable development of societies. Acquisition of accurate farming information such as estimation of the area allocated to each crop type, crop development status, crop statistics computation, or crop production forecasting is an essential for sustainable agriculture and food security. Precision agriculture is a management strategy that integrates information and communication technologies with the agricultural industry. Several methodologies for crop monitoring and extraction of useful information such as seeding stage, crop status, and harvesting time, provide valuable data for different applications, e.g., for irrigation and fertilization practices and plant anomalies recognition. Among them, remote sensing techniques contribute to assess, map and monitor cultivated areas, leading to significant developments in agricultural field in recent years (Abdikan et al., 2018; Canisius et al., 2018). Agricultural targets are very dynamic and time-critical throughout the growing season, and thus satellite-based techniques are useful tools for the collection of crops phenological and statistical information. In particular, microwave remote sensing has been extensively used for agriculture purposes, due to the penetration capability of microwave radiation into vegetation canopy and the sensitivity to natural targets' water

* Corresponding author.
E-mail address: rouhollah.nasirzadehdizaji@std.yildiz.edu.tr (R. Nasirzadehdizaji).

https://doi.org/10.1016/j.compag.2021.106118
Received 29 August 2020; Received in revised form 11 March 2021; Accepted 17 March 2021

content (Ulaby, 1981; Veloso et al., 2017; Zhou et al., 2017).

RADAR (Radio Detection And Ranging) instruments onboard airborne or space-borne satellites have also a high potential for providing useful information on agricultural crop status in most weather conditions. The signals returned towards the satellite antenna, which is influenced by vegetation and soil properties, fall under the two main principles of geometric structure and dielectric properties (Wooding et al., 1995). Agricultural radar applications allow the analyst to extract extra information about crop conditions and characteristics, contributing to crop production forecasting, crop mapping and monitoring, assessment of declarations for fraud control, and further investigations (Steele-dunne et al., 2017).

The potentiality of using sigma nought (σ^0) maps and interferometric synthetic aperture radar (InSAR) coherence for forestry and agriculture monitoring has been individually investigated in different studies. As one of the first and fundamental studies on microwave remote sensing for agricultural applications, the work in Ulaby (1981) demonstrated a significant correlation between radar signatures and vegetation variables over the specific fields. Later on and with the launches of ERS-1/2, JERS-1, and RADARSAT satellites, substantial progress has been achieved in interpreting multi-temporal radar signatures of crops in terms of vegetation parameters estimation (Macelloni et al., 2001), crop cycles monitoring (Saich and Borgeaud, 2000), crop mapping and classification (Lee et al., 2001). Multi-temporal, multi-polarization, and multi-frequency synthetic aperture radar (SAR) images analysis is the most prominent characteristic of radar remote sensing to determine temporal variations of the crop phenology identify changes in crop structure (Stankiewicz, 2006). The monitoring of rice fields' phenological variations was investigated (Lopez-Sanchez et al., 2012), using dual-pol X-band TerraSAR-X data. They proposed a simple procedure to estimate the phenological stage by analyzing the scattering mechanisms and polarization effects of the different phenological stages. From the interpretation of rice and the ground measurements' radar response, they obtained satisfactory compromise in terms of the phenology of the rice. Sensitivity analysis of multi-temporal polarimetric Sentinel-1 SAR images was used in (Nasirzadehdizaji et al., 2019) to study the crop growth stages and the temporal backscatter changes for different crop types. From the backscattering analysis, they found that useful information about crop status can be extracted according to the given changes in backscatters, such as estimating irrigation and harvesting time. A new vegetation index from dual-pol (DpRVI) SAR data has been recently introduced by Mandal et al. (2020), who compare the cross and co-pol scattering ratio, dual-pol Radar Vegetation Index (RVI), Polarimetric Radar Vegetation Index (PRVI), and the Dual Polarization SAR Vegetation Index (DPSVI) with temporal analysis of crop biophysical variables at different phenological stages. Compared with other indices, the results showed that the DpRVI index has high correlation and good retrieval accuracy with the selected crop types' biophysical parameters.

Earlier, the InSAR coherence-based analysis application for assessing vegetation parameters to detect abrupt changes of vegetation cover in forest regions and study the deforestation effects was performed by Zebker and Villasenor (1992). The various decorrelation sources of the interferometric radar echoes were analyzed to identify the topographic variations of the surfaces covered by the vegetation. The study results showed that using repeat-pass interferometry for the generation of height maps of densely vegetated areas is a practical approach. The InSAR-based approaches have been applied for agricultural monitoring to compare interferometric coherence for mowed grasslands with grasslands covered by vegetation (Zalite et al., 2014). The authors pointed out that coherence increases with grass removal and found a robust correlation between the vegetation height and wet above-ground biomass with the temporal coherence. However, the correlation between the backscattering coefficient and the wet biomass, as well as the height of grass, appeared insignificant. The importance of the meteorological effects in the interpretation of InSAR coherence was studied (Askne and Santoro, 2003). Moreover, the relationship between the coherence at C-band and grasslands mowing events and temporal decorrelation induced by precipitation in Central Estonia was investigated (Tamm et al., 2016). In their study, the feasibility of interferometric coherence for mowing detection was assessed, and the various factors affecting the coherence, such as farming activities and meteorological conditions, were determined.

For the retrieval of vegetation parameters and the monitoring of farming activity, crop growth, and soil moisture variations, the work (Wegmüller and Werner, 1997) presented an InSAR-based application using ERS-1 SAR data pair over agricultural and forested test areas. Their results showed that as the crop grows, the interferometric correlation decreases, while the post-harvest indicates a high correlation. They also achieved high accuracies of forest mapping (90%) using the elevation map generated from the same SAR data pair and validated with a usual digital forest map. Blaes and Defourny (2003) investigated the correlation between ERS-1/2 SAR Tandem interferometric coherence and different crop type parameters (crop height, canopy coverage, etc.). Coherence values derived from ERS SAR image pairs' analysis compared to the field measurements of crop growth indicated high coefficients of determination (R^2). According to their findings, the backscattering coefficient is more sensitive to the soil moisture variations than the coherence signal. A recent research (Mestre-Quereda et al., 2020) investigated the contribution of Sentinel-1 coherence and intensity data and the impact of polarization for generating thematic maps for crops. They concluded that the complementary use of coherence and intensity data provide high accuracy in crop classification applications.

Although the different agricultural applications of SAR systems based on the analysis of the intensities of backscattered signals have been investigated throughout various studies (Vreugdenhil et al., 2018, Khabbazan et al. 2019), the potential of using SAR backscattering jointly with the coherence for agricultural crop monitoring has not been thoroughly investigated. Our work aims to give more insights into the synergic use of SAR imagery's coherence and intensity values to analyze the biophysical variations of different crops during the growing season and point out SAR remote sensing capability for agriculture monitoring. To perform a comprehensive investigation, this study focuses on the exploitation of Sentinel-1 data acquired in different tracks, passes (ascending and descending) and polarization (VV and VH) for the monitoring of different crop types (i.e., maize, sunflower, and wheat) in TIGEM (State General Directorate of Agriculture Enterprise) farm of Konya, central Turkey.

2. Materials and methods

Within the context of this work, we investigate the relationships (i) between the interferometric coherence calculated from different pass directions, multi-track of 12- and 6-day Sentinel-1 SAR image pairs in VV and VH polarization, and (ii) between the SAR backscatter values determined from the multi-temporal SAR images and the different crop type's growth stages (i.e., sowing, growing, and harvesting). For validation purpose, field surveys were systematically conducted in the study area.

2.1. Site description

As one of the top ten largest agricultural producers globally, Turkey's agriculture plays a critical socio-economic role for the country. Due to its great variety in geomorphology, topography and climate, a large percentage of the country is allocated to the agricultural land, and now a significant number of the population is employed in agriculture. Turkey's central Anatolia region and the Konya basin (38°40′ N, 32°26′ E) are among the most prone areas to agricultural activities. The study area terrain is relatively flat with a gentle slope (3–6%). The basin is predominantly used for agricultural purposes due to its low contents of organic matter (1.12–1.74%) and soil texture, which consists of the medium structure of clayed loam and loamy, slightly alkaline, and saltfree (Basaran, 2017). Fig. 1 shows the study site's location and illustrates the footprints of the used Sentinel-1 images with related track numbers, satellite flight, and Line of Sight (LOS) directions.

2.2. Field surveys

In total, 20 agricultural fields ranging between 0.5 and 18 ha of fields' sizes for maize (9 fields), sunflower (6 fields), and wheat (5 fields) with different crops patterns were selected for our study, and four in situ surveys were conducted during the spring-summer agricultural season of the year 2016. Field observations provide information regarding the soil properties/moisture and irrigation status, the sowing and seeding times, crop growth stages, crop parameters (i.e., crop height, plant cover, and row) and characteristics, and harvesting time of the crops. Specific growth stages such as leaf development, tillering, stem elongation, booting, heading, flowering, and maturity have been determined to identify plants' phenological development stages. According to field campaigns, maize and sunflower generally are planted in mid-May and harvested at the mid to the end of September in the study area. Winter wheat is seeded at the end of the previous October or the beginning of November and harvested at the end of July. The variability of development stages for maize, sunflower and wheat in the study area is presented in Fig. 2.

2.3. Sentinel-1 SAR datasets

Sentinel-1A and Sentinel-1B are two SAR C-band imaging satellites of the Copernicus Program, launched into orbit on 3 April 2014 and 25 April 2016, respectively. Sentinel-1A and Sentinel-1B are twin satellites, with many compatibilities as to their imaging geometries, and the common orbital plane with a 180° phase difference along with small orbital baselines. The constellation offers global coverage with a revisiting time of 6 days over Europe and 12 days in the rest of the world, providing unique opportunities for systematic Earth surface monitoring and change detection applications. Data acquired in both ascending and descending orbit passes, and in dual polarization (VV and VH), were collected for this study. For the interferometric coherence and the multitemporal SAR backscattering data analysis, a total of 66 Single Look Complex (SLC) interferometric wide (IW) swath SAR images (33 ascending and 33 descending) were acquired throughout the investigated growth season of the study area and adequately processed. Before the Sentinel-1B launch, data were obtained every 12 days for each orbit in the study area. Since the end of September 2016, the revisit period has been reduced to 6 days due to its placement into orbit. An overview of datasets with relative characteristics is shown in Table 1. The acquisition dates for each orbit, from April to October 2016, are given in Table 2.

2.4. Data processing

The processing steps used for obtaining interferometric coherence and SAR backscatter (σ^0) maps are shown as flow-chart in Fig. 3. The interferometric SAR processing is performed using the open-source Generic Mapping Tools SAR (GMTSAR) InSAR processing package (Sandwell et al., 2011). The InSAR analysis relies on estimating the phase difference given by the complex conjugate product operation between two SAR images (i.e., master and slave). A co-registration between the master and the slave scenes is applied by taking into account accurate orbital information and a Digital Elevation Model (DEM) of the area (Pepe and Calò, 2017). The latter is also used to compute and subtract the topographic phase component from the interferograms and generate the differential SAR interferograms (i.e., related to the ground displacement).

Moreover, spectral filtering is applied to mitigate the noise in the computed interferograms. Also, coherence maps are generated as in detail explained in Section 2.5. Finally, the interferometric products are geocoded, i.e., converted from radar to geographic coordinates (Sandwell et al., 2011).

Regarding the amplitude data processing, multi-polarized SAR images are radiometrically calibrated to convert the digital number (DN) values of each pixel into the relevant sigma nought measure, i.e., the surface backscattering coefficient. As a general phenomenon in all SAR imaging systems, and due to the interference of the backscattered signal from the target, SAR images inherently have a grainy salt and pepper pattern called speckle, reducing the imaging capability for further analyses. It degrades the radiometric quality of data and makes it difficult for the analyst to interpret. We applied Refined Lee (with a seven × seven window size) filter to remove speckle in SAR images as the most accurate and useful filter for crop mapping (Lavreniuk et al., 2017).

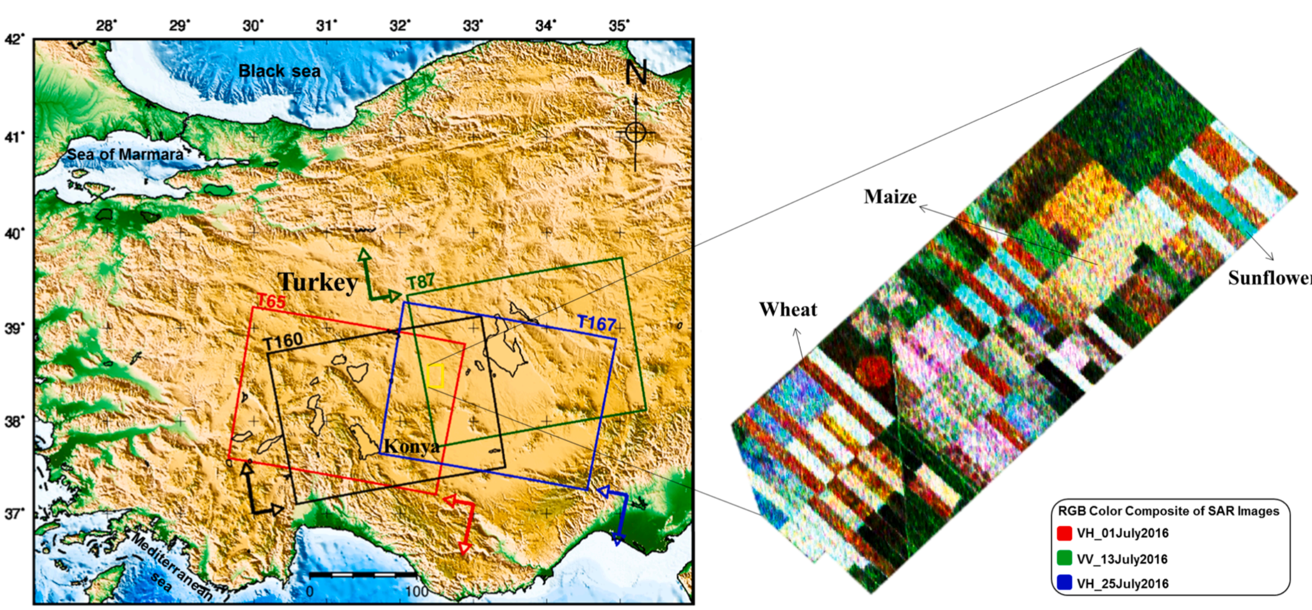

Fig. 1. Location map of the study area. The investigated fields have been shown in the RGB color composite of SAR images. The colored boxes show the Sentinel-1 imagery footprints where *T* indicates the tracks; the satellite flight direction and the LOS are represented by the perpendicular longer and short arrows, respectively. The yellow box shows the test site which is approximately 40 km^2. (For interpretation of the references to color in this figure legend, the reader is referred to the web version of this article.)

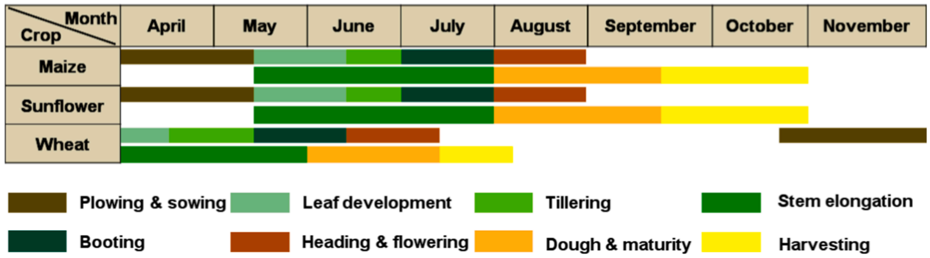

Fig. 2. Seasonal stages for maize, sunflower and wheat in the investigated fields.

Table 1
Characteristics of Sentinel-1 datasets used for the study.

Orbit Number	Satellite pass	Acquisition Time (UTC)	Swath	Incidence Angle (°)	Resolution (m)	
					Slant Range	Azimuth
87	Ascending	15:42	IW3	43.1	3.5	22.6
65	Descending	03:58	IW1	32.9	2.7	22.5
160	Ascending	15:49	IW3	43.1	3.5	22.6
167	Descending	03:50	IW3	43.1	3.5	22.6

Table 2
Acquisition dates for different orbits.

Orbit Number	65	87	160	167
Month		Acquisition dates		
April	2,14,26	3,15,27	8,20	9,21
May	8	9,21	2,15,26	3,15,27
Jun	1,13	2,14	7	8
July	7,19,31	8,20	1,13,25	2,14,26
August	12,14	1,13,25	6,18,30	7,19,31
September	5,17,29	6,18,30	23[a],29	12,24[a],30
October	5,11	6,12	2,11	6,12

[a] From these dates on, for 160 and 167 orbit numbers, acquisitions were made every 6 days.

Although the speckle in the image decreases as the filter's window size increases, this may result in the loss of details (e.g., edges or borders) in the image. Therefore, the SAR images' pixels are filtered using an optimal window size of 7 × 7 for retaining details. SAR image is acquired in slant looking geometry, and hence the time of the signal to travel to the Earth's surface and back to the sensor is distorted, causing geometric shifts in the image. Range-Doppler terrain correction shifts all pixels to their correct locations according to an input DEM. A Range-Doppler terrain geometric correction using SRTM 3-arc-second DEM data increases the location accuracy of the images. The σ^0 values are converted into a logarithmic scale (dB). Finally, co-registration was applied to increase the spatial homogeneity between the integrated stack images. These operations have been performed using open source tools of Sentinel Application Platform (SNAP) software (SNAP-ESA, 2020).

The mean backscattering values of pixels were computed from field-based polygons of the different crop types and the correlation with the field measurements was evaluated by analyzing multi-temporal SAR images for each field. The mean backscatter signature of the selected pixels from the polygons for all patterns as well as the variation of the backscatter values for each crop types and each pattern in the timeframe of the study, in each orbit passes (ascending and descending) and polarization modes (VH and VV) were interpreted (see Section 3). We have calculated all the possible image pairs to get the full coherence matrix, as shown in Figs. 4 and 5. The coherence analysis shows that pairs of consecutive images in time have the highest coherence. This is due to relatively low changes in the scatterers over the agricultural fields between the two acquisitions in 12 days.

2.5. InSAR coherence estimation

Coherence represents the absolute value of the (complex) cross-correlation index between a couple of SAR images, and it provides useful information on the amount of noise corrupting the (multi-looked) interferograms (Ferretti et al., 2007; Perissin and Wang, 2012). The expression of an SLC image in the complex notation is given by:

$$\mathrm{C}(\rho,\mathrm{a}) = \mathrm{A}(\rho,\mathrm{a})\mathrm{e}^{\mathrm{i}\phi(\rho,\mathrm{a})} \tag{1}$$

where the complex-valued SAR signal $C(\rho,\ a)$ is represented by its amplitude $A(\rho,a)$, and phase $\phi(\rho,a)$. $i = \sqrt{-1}$ is the imaginary unity, and ρ and a represent the range and the azimuth coordinates of the generic SAR pixel of the focused SLC image, respectively. Once the two interfering SAR images are co-registered the complex interferogram is achieved, pixel-by-pixel, by cross-multiplication of the first SAR image by the complex conjugate of the second image (Rosen et al., 1996) as:

$$(\rho,a)C_1^*(\rho,a) = A_1(\rho,a)A_2(\rho,a)e^{i(\phi_2(\rho,a)-\phi_1(\rho,a))} = R(\rho,a) + iI(\rho,a) \tag{2}$$

where C_1 and C_2 are the master (the reference) and slave (the repeat) SLC images, respectively, A_1 and A_2 are master and slave amplitudes, and ϕ_1 and ϕ_2 are master and slave phases, respectively. The asterisk (*) denotes complex conjugation. R and I represent the real and imaginary components of the complex interferogram, respectively. The interferometric phase is the phase difference between the two SLC images (Ferretti et al., 2007):

$$(\phi_2 - \phi_1) = \tan^{-1}\left(\frac{I}{R}\right) \tag{3}$$

Considering complex SAR image pairs that contain both amplitude and phase information, a measure of the phase noise corrupting an interferogram is given by the interferometric coherence (γ) between the two complex co-registered SLC images. It is defined as the absolute value of the (complex) cross-correlation factor between the two interfering SAR signals (Bron and Wolf, 2007):

$$\gamma = \frac{|\langle C_1 C_2^* \rangle|}{\sqrt{(\langle C_1 C_1^* \rangle \langle C_2 C_2^* \rangle)}} \tag{4}$$

where | | indicates the absolute value, * indicates complex conjugation and angle brackets < > represent the ensemble statistical average operation, which is performed by spatially averaging the signals over a small window with a specific size (a few pixels in range and azimuth). A

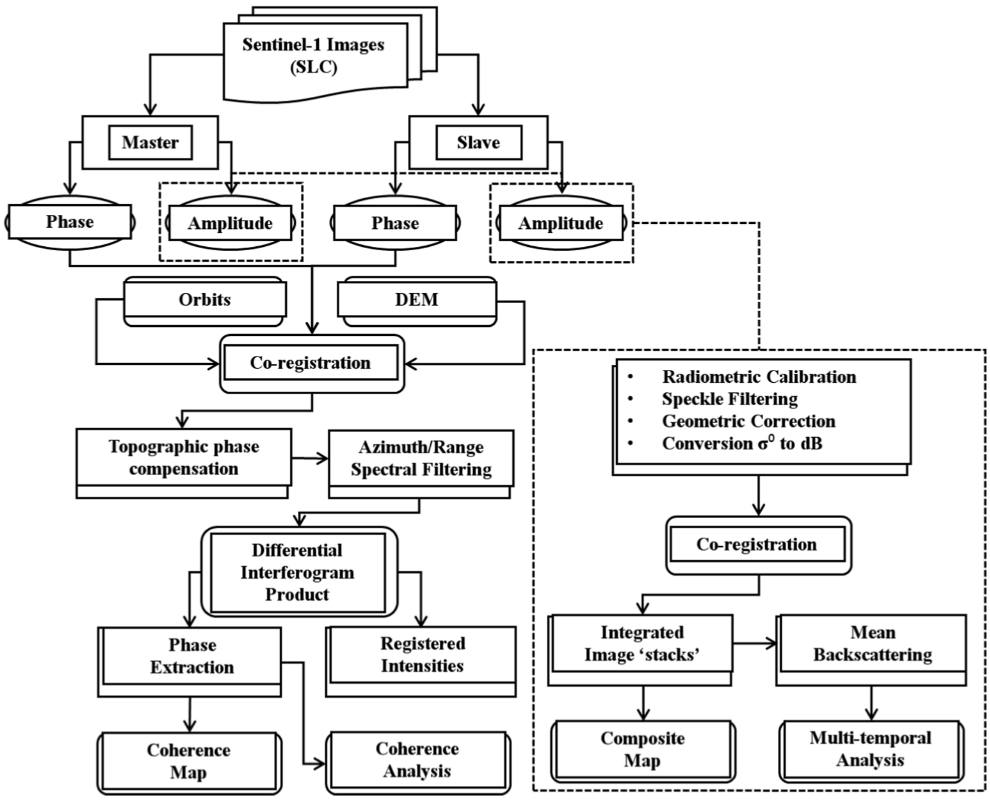

Fig.3. General pre-processing workflow schema for Sentinel-1 SLC SAR images.

filter is also applied to reduce the difference in radar impulse response perceived by sensor path from the same piece of ground. To enhance the quality of the amplitude image of the single-look Sentinel-1, which has 5 m resolution in range and 20 m in azimuth, and to obtain a spatial averaging coherence, different window sizes (e.g., 5 × 5 or 7 × 7 pixels) are applied based on the corresponding spatial resolution of the image. The coherence ranges from 0 in the case of complete decorrelation (the interferometric phase is just noise) to 1 if the two signals are fully correlated (complete absence of phase noise). When the scatterers' position and physical properties within the averaging window are the same for the two observations, the coherence reaches the maximum value. In contrast, any differences in the scatterers' position or properties in the interval between the two observations cause the phase difference of two backscattered signals and thereby cause the coherence value to decrease. An interferogram image represents the phase difference of two SAR images, and the phase is given modulus 2π.

2.6. Decorrelation sources

A decrease in the coherence or decorrelation can have several sources. Physical changes in the terrain and changes in the position or characteristics of the scatterers of the surface cause the non-conformity of the two acquisitions' properties over time and are expressed by the temporal decorrelation ($\gamma_{thermal}$) (Just and Bamler, 1994). The difference in the incidence angles between the two observations gives rise to the geometric or spatial baseline decorrelation ($\gamma_{spatial}$). Other sources are represented by the thermal or system noise decorrelation ($\gamma_{thermal}$or γ_{SNR}) due to the characteristics of the system (e.g., antenna characteristics and gain factor); the volume decorrelation (γ_{vol}) which results by volume scattering; the Doppler centroid decorrelation (γ_{DC}) which arises by the differences in the Doppler centroids between the two observations; the processing induced decorrelation ($\gamma_{processing}$) that is the error from the selected algorithms (e.g. for co-registration and interpolation); the bias decorrelation (γ_{bais}) caused by the averaging window size. The total coherence (γ_{total}), which is calculated from Eq. (5), is given as the multiplication of the aforementioned correlation terms (Zebker and Villasenor, 1992):

$$\gamma_{total} = \gamma_{temporal}\gamma_{spatial}\gamma_{thermal}\gamma_{vol}\gamma_{DC}\gamma_{processing}\gamma_{bais} \tag{5}$$

Our study focuses on the temporal and the system thermal noise decorrelation terms, by neglecting the other contributions since the perpendicular baselines of the interferograms and the variations of the incidence angles across the scene, in our case, are minimal. The temporal decorrelation ($\gamma_{\mathrm{temporal}}$) is due to rapid changes in the scatterers over the agricultural fields during the acquisitions' crop growth season. The system noise decorrelation is defined as:

$$\gamma_{SNR} = \frac{SNR}{SNR + 1} \tag{6}$$

where SNR is the image signal-to-noise ratio (Ferretti et al., 2007). It can equivalently be expressed as:

$$\gamma_{SNR} = \frac{1}{\sqrt{\left(1 + SNR_{master}^{-1}\right)\left(1 + SNR_{slave}^{-1}\right)}} \tag{7}$$

where SNR_{master} andSNR_{slave} represent the signal-to-noise-ratio for the master and slave images, respectively. The expression of the SNR for a given SAR image is as follows:

$$SNR_{sat} = \frac{\sigma^0_{sat} - NESZ_{sat}}{NESZ_{sat}} \tag{8}$$

The backscattering coefficient for different acquisitions and $NESZ_{sat}$ is a noise parameter that can be estimated using look-up tables available in the Sentinel-1 metadata.

3. Results and discussion

Multi-pass Sentinel-1 data are used to calculate interferometric

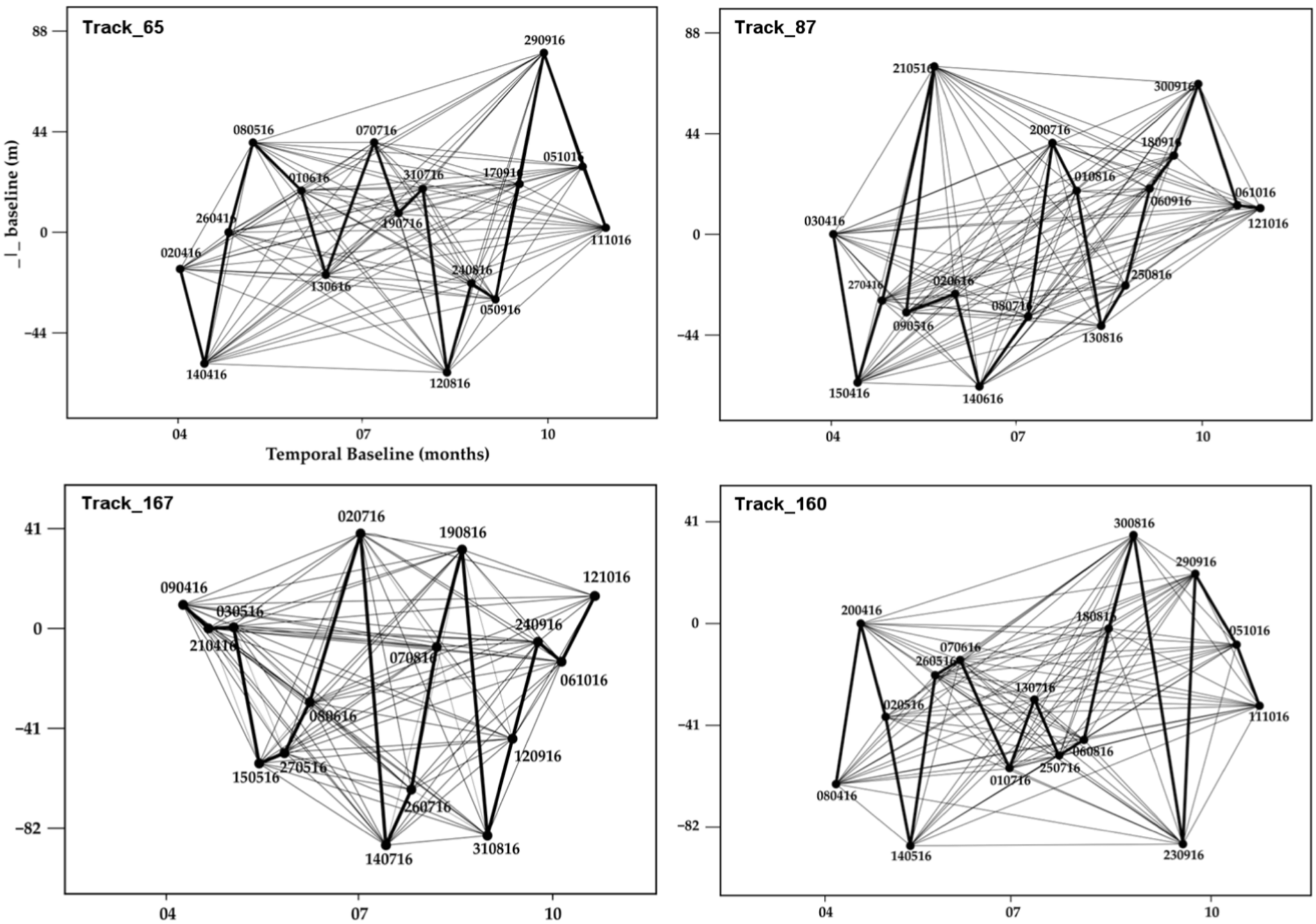

Fig. 4. Baseline configurations related to all tracks in both ascending and descending pass directions for VV polarization. The bold lines in each track represent the baselines between the consecutive images in time (STBs) used for coherence analyses. The horizontal axis is the time of acquisitions, and the vertical axis shows the perpendicular baseline. Lines correspond to interferograms, and nodes correspond to SLC images with acquisition date (in dd-mm-yy format).

coherence and SAR backscatter values for the investigated agricultural field with different crop types. In this section, the relationships between the different phenological stages (sowing, growth, and harvesting) of the crops and the radar coherence and SAR backscattering are investigated. The results show that coherence values are high at the early stage before plowing and seeding and sharply decrease with the starting of the crop growth at mid-stage. During the crops' growing phase, the values stay low and slightly similar for each field and crop types. The coherence values get significantly higher at a later stage after crop harvesting and reaping the crops' remnants.

Compared with the ascending pass direction, the coherence value is high for each field with the same crop type in descending orbit. In terms of multi-temporal analysis, the SAR backscatter values start increasing after plowing and sowing and leaf development until reaching the crops to the mid growing stages. In this stage and when the plant reaches the full inflorescence emergence, the values remain constant and/or show minor increases. When the crop is ripe, the backscatter values start to decrease and become weak. They reach the lowest level following the harvesting and reaping the remnant of the plants from the ground. The highest mean coherence and backscatter values of maize, sunflower, and wheat for different growth stages from four different tracks and pass directions are shown in Table 3. In comparison to VH, the VV polarization shows higher values for both coherence and backscattering. Hence, the values shown in Table 3 are related to the VV polarization.

3.1. Coherence estimation, backscatter analysis and their relation with crop growth

For each crop type in 20 fields, vegetation parameters, including sowing, growth, and harvesting stages, are recorded in the different field measurements. Due to the simultaneous planting of maize and sunflower in the study area, the coherence value is maximum for both crops at the end of March and early June after plowing the fields and seeding the crop. The mean interferometric coherence values become maximum for the maize ($\gamma = 0.47$), and sunflower ($\gamma = 0.49$) in VV polarization for both ascending and descending orbits. The value starts to decrease with the growth of the plants. At the beginning of July, once the ground is covered by the plant and the soil effects eliminated from the radar backscatter, it reaches its lowest value for maize and sunflower ($\gamma = 0.08$ and $\gamma = 0.09$, respectively). However, before the crops reach their harvesting time, an increase is observed in the coherence values for maize and sunflower, probably due to weather conditions, e.g., precipitation. The coherence again starts to get higher in late September and October for maize ($\gamma = 0.51$) and sunflower ($\gamma = 0.50$), respectively, when the crops are close to their harvesting time.

Since wheat is seeded in late October of the previous year and the SAR data analysis starts at the beginning of April when the crop is in its heading stage, coherence values are low ($\gamma = 0.07$) until the harvesting time, and after that, there is a sharp increase in estimated coherence ($\gamma = 0.42$) at the end of June and early July. Mean coherence values for maize (9 fields), sunflower (6 fields), and wheat (5 fields) for ascending and descending passes in different tracks and polarizations are given in Figs. 6–8. In comparison with the ascending orbit, the interferometric

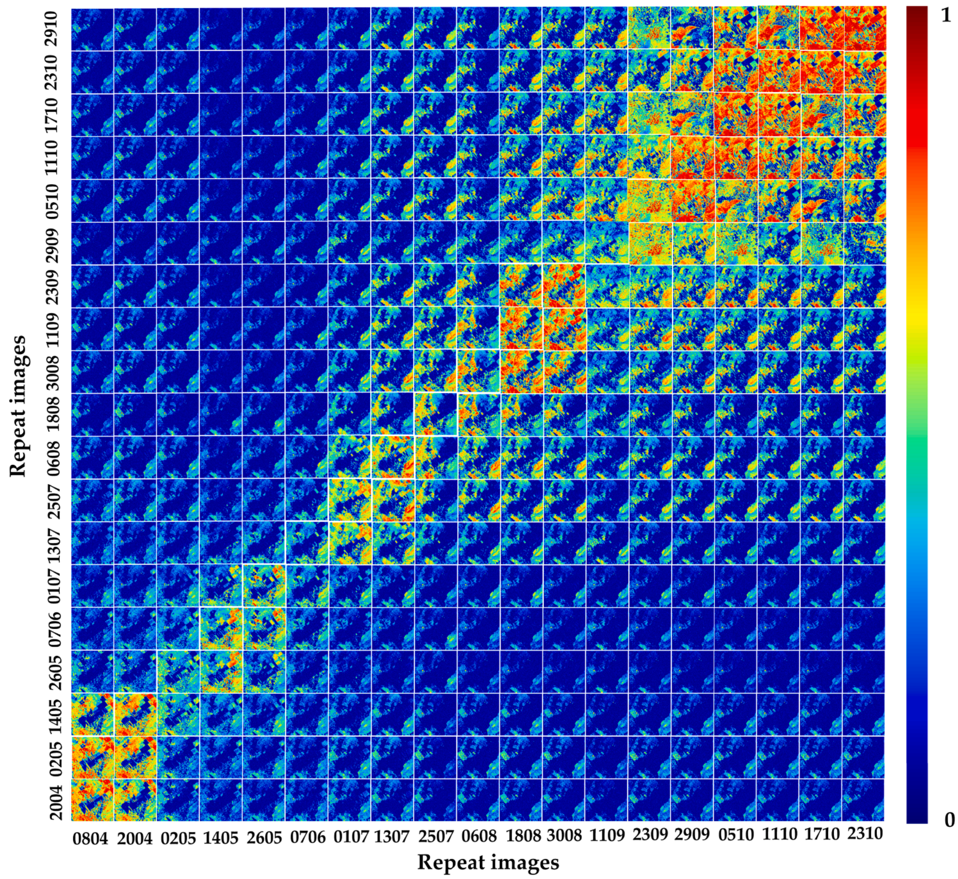

Fig. 5. Matrix representation of the whole set of generated InSAR coherence maps for track number 160. Note that all possible interferometric data pair combinations have been considered. The X and Y axes represent the SAR image acquisition date (in dd-mm format) for the related track. Note coherence is higher in consecutive image pairs during the crop growth stages.

Table 3
Mean coherence and backscatter values of maize, sunflower and wheat for different growth stages.

Status	Maize		Sunflower		Wheat	
	γ	σ^0 (dB)	γ	σ^0 (dB)	γ	σ^0 (dB)
Early stage						
Plowing & sowing	0.49	−14.79	0.73	−13.12	–	–
Leaf development	**0.47**[a]	−13.52	**0.49**	−8.70	0.16	−17.15
Mid stage						
Tillering	**0.08**	**−9.18**	**0.09**	−7.46	0.12	−14.36
Stem elongation	0.10	−10.06	0.11	−5.87	**0.07**	−14.42
Booting	0.10	−10.26	0.12	**−5.24**	0.09	−13.21
Later stage						
Heading & flowering	0.22	−11.13	0.51	−10.51	0.17	**−10.05**
Dough & maturity	0.13	−11.18	0.29	−12.17	0.19	−12.16
Harvesting						
Harvesting	**0.51**	−14.79	**0.50**	−12.79	**0.42**	−14.58
Post-harvesting	0.63	−15.86	0.71	−13.46	0.62	−17.37

[a] The bold values indicate the min and max coherence values during the crops growth stages.

coherence values result in higher in all crop types for the descending dataset. Between the VV and VH polarization, much better coherence values are estimated using VV acquisitions till the end of the leaf development stages. This is probably due to the sensitivity of co-polarization over the enhanced volume scattering of vegetation and lack of canopy penetration of VV polarization (Manavalan, 2018). However, similar values are obtained for both acquisitions during the crops growth stages and before harvesting time. The temporal profiles of σ^0 in VH and VV polarization for maize, sunflower, and wheat crops during the observed period are also illustrated in Figs. 6–8 to make the comparison. The analysis shows that, in both ascending and descending orbits, the σ^0 values are higher in VV than in VH polarization and high intensity and the change in values is considerable. In the figures, the different crop growing seasons are also reported to investigate the relationship with the SAR backscatter coefficient's temporal variations.

After plowing and sowing, with the growing of the crops and the rapid changes in leaf geometries and physical structure of the crops, due to the sensitivity of SAR to the geometrical characteristics of the targets an increase of the σ^0 values is observed till the crops reach to the mid growing stages (tillering, stem elongation and booting stages). The highest mean σ^0 values in this stage for the maize, sunflower and wheat are −9.18 dB, −5.24 dB and −10.05 dB, for ascending pass direction in VV polarization. For the maize, during its mid-stages and when the maize reaches at the full inflorescence emergence the backscatter values remain constant. At this stage, the σ^0 values slightly continue to increase for the sunflower until the inflorescence reaches up to the full size. Regarding the winter wheat, similarly as for the coherence, the backscatter analysis starts at the beginning of May when the crop is in its leaf development stage. The SAR backscatter values indicate continuous stability in this stage and before the later stage (heading and flowering, dough, maturity, and harvesting time). Although in comparison with VH polarization in terms of backscatter values, the VV polarization indicates higher intensities, instead the sensitivity to the crop status changes of the VH polarization is much higher in the backscatter profiles stage. The values start to increase at the heading time. The increases in the intensity in this stage happen maybe due to the wheat hyacinth structure. However, it decreases when the wheat is ripe, and the harvesting comes, similarly to the sunflower. For the maize, at the late stage and during the heading, maturity and reaching to the harvesting time, the σ^0 remains

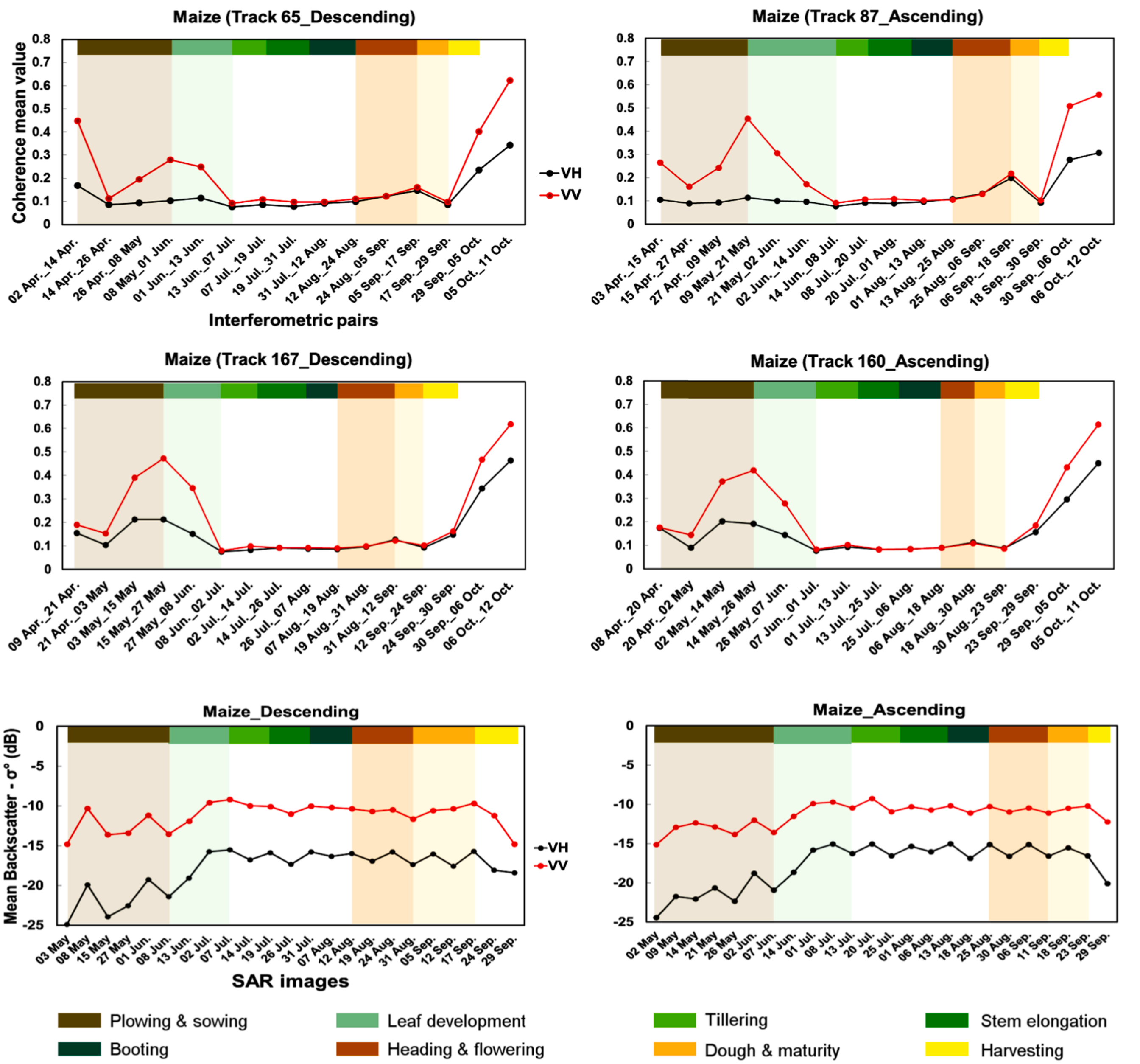

Fig. 6. Maize: mean coherence and SAR backscatter values computed over nine fields *vs.* seasonal growth stages, for VH and VV datasets acquired in both ascending and descending orbits. X-axis reports the data pairs used for coherence maps generation.

constant until the crop is harvested. Following the harvesting and removing of the crops' remnant from the ground, the backscattering values decrease in all crop fields because of the interactions between the SAR signal and the soil.

The results show a significant correlation between the field observations and the estimated coherence and backscatter values in terms of identifying different phenological stages of the selected crop types in the study area. Thereby, this enables us to derive a method for monitoring and estimate the growing status of the different agricultural fields by defining thresholds for SAR coherence and backscattering over extended scales where field observations are time-consuming, excruciating and costly (see Table 4).

Interferometric coherence analysis indicates a significant difference between VV and VH polarizations for maize, sunflower, and wheat in coherence values (ϒ) at the post-harvesting stage. The values are very high for VV polarization in comparison to the VH in this stage. The maximum differences in values between the two polarizations are 0.28, 0.37, and 0.48 for maize, sunflower, and wheat. Several parameters can be effective in making this difference. The first reason that may cause the discrepancy can be due to the phase difference between the two polarizations, where the phase velocity of H and V waves differs within the target due to a delay in time (McNairn et al., 2002). The differences can also arise from various sources including variations in harvesting techniques, amount and height and orientation of residue, and soil and residue moisture levels at the harvested fields that affect radar backscatter. Moreover, depending on the residue structure that mainly is vertical due to the cutting the crops with such a mot mower, residues (e.g., stems) act as a combination of single bounce backscatter, therefore, the co-polarized phase differences support to lay out the dominant scattering mechanism.

The profiles indicate an evident decrement in early-season backscatter, followed by an increase with crop leaf development, and until the time of grain fill. The values start decreasing with the maturity and ripening of the crops. A subsequent significant increase happens

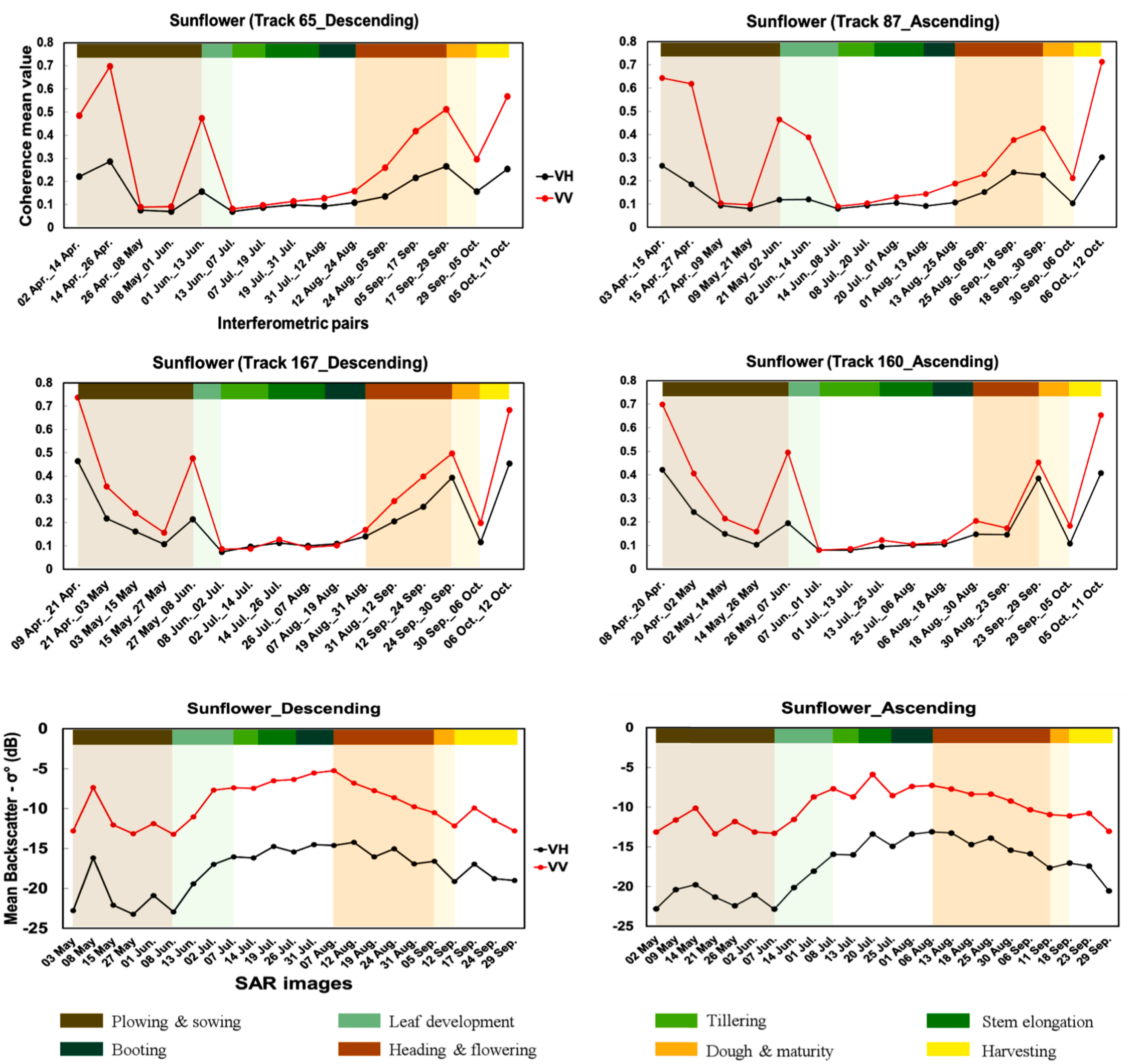

Fig. 7. Sunflower: mean coherence and SAR backscatter values computed over six fields *vs.* seasonal growth stages, for VH and VV datasets acquired in both ascending and descending orbits. X-axis reports the data pairs used for coherence maps generation.

following the harvest. Fig. 9 shows the changes in maize, sunflower, and wheat backscatters and mean backscatter temporal profiles for growing seasons of all fields for the different crop types in the study area. There are some notable differences between the averaged backscatter temporal profiles of the different crop types. Since maize reaches to its end of leaf development and full size on day 160, during the mid-stage (i.e., stem elongation and booting) the values continue to be constant or show minor changes. This is the same for wheat when its leaves completely unfold. In this stage and when sunflowers' leaf development was completed on day 190, a sharp backscattering decrease was observed. The discrepancy in backscattering might be due to the difference in leaves structure and maize and wheat geometry as a narrow-leaf and sunflower as a broad-leaf crop.

4. Conclusions

In this study, multi-temporal and multi-polarization analyses based on interferometric coherence and SAR backscattering of Sentinel-1 datasets have been carried out for crop growth monitoring in the Konya agricultural region, Turkey. By exploiting data and information collected during field surveys, the relationships between SAR products (coherence and backscattering) and crop growing seasons are investigated. A significant correlation between the different phenological stages (sowing, growth, and harvesting) of the crops and the radar coherence is found. In particular, the analysis pointed out that, before plowing and after seeding, the coherence values are high, but sharply decrease once the crops' growing season starts. During this stage, the coherence values remain low and slightly similar for each field and crop type. The coherence values significantly increase after crop harvesting and reaping the remnants of the crops. Compared with the ascending dataset, it is observed that coherence values are generally high for each field with the same crop type by using data acquired along the descending orbit. The increase of values for VV polarization is higher compared with the VH polarization for different crops. It can be inferred from the performed analysis that the agriculture activities related to plowing, seeding, and harvesting the crops have a significant impact on

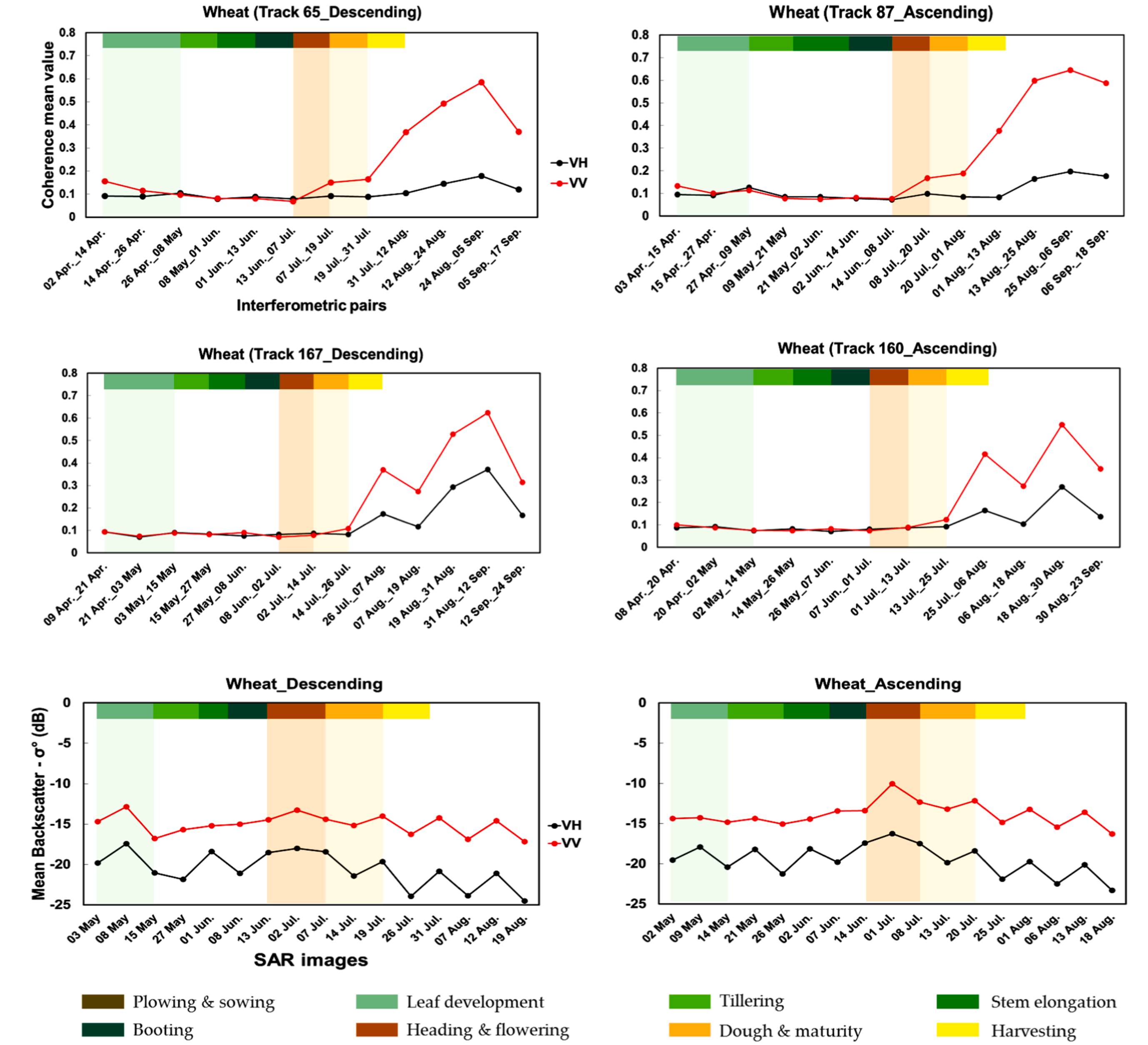

Fig. 8. Wheat: mean coherence and SAR backscatter values computed over five fields *vs.* seasonal growth stages, for VH and VV datasets acquired in both ascending and descending orbits. X-axis reports the data pairs used for coherence maps generation.

Table 4
Thresholds identification for coherence and backscattering values for different growth stages of maize, sunflower and wheat.

Stages	Maize		Sunflower		Wheat	
	γ	σ^0 (dB)	γ	σ^0 (dB)	γ	σ^0 (dB)
Early stage	0.3–0.4	−15 to −13	0.3–0.6	−13 to −9	0.1–0.3	−17 to −15
Mid stage	0.1–0.15	−11 to −9	0.1–0.15	−7 to −5	0.1–0.15	−15 to −13
Later stage	0.15–0.3	−12 to −11	0.25–0.35	−12 to −10	0.15–0.2	−12 to −10
Harvesting	0.3–0.5	−14 to −12	0.35–0.5	−13 to −12	0.2–0.4	−16 to −14
Post-harvesting	>0.5	<−15	>0.6	<−13	>0.4	<−16

the InSAR coherence values. This is confirmed by the SAR backscattering based-analysis, highlighting a high correlation between the different growth stages of the crops and the SAR backscatter. In particular, the results show that, at the early and later stages of the crops, the mean backscattering values are low and increase with the crops growing until the plants reach the full size. Values remain constant after the leaf development and following the harvest and decrease to the lowest values due to SAR scattering interactions and the ground.

Moreover, SAR backscattering values, and their temporal variations, result to be higher when using data acquired in VV than in VH polarization. This study demonstrates that Sentinel-1 SAR data can be useful for crop growth monitoring. Particularly, interferometric coherence

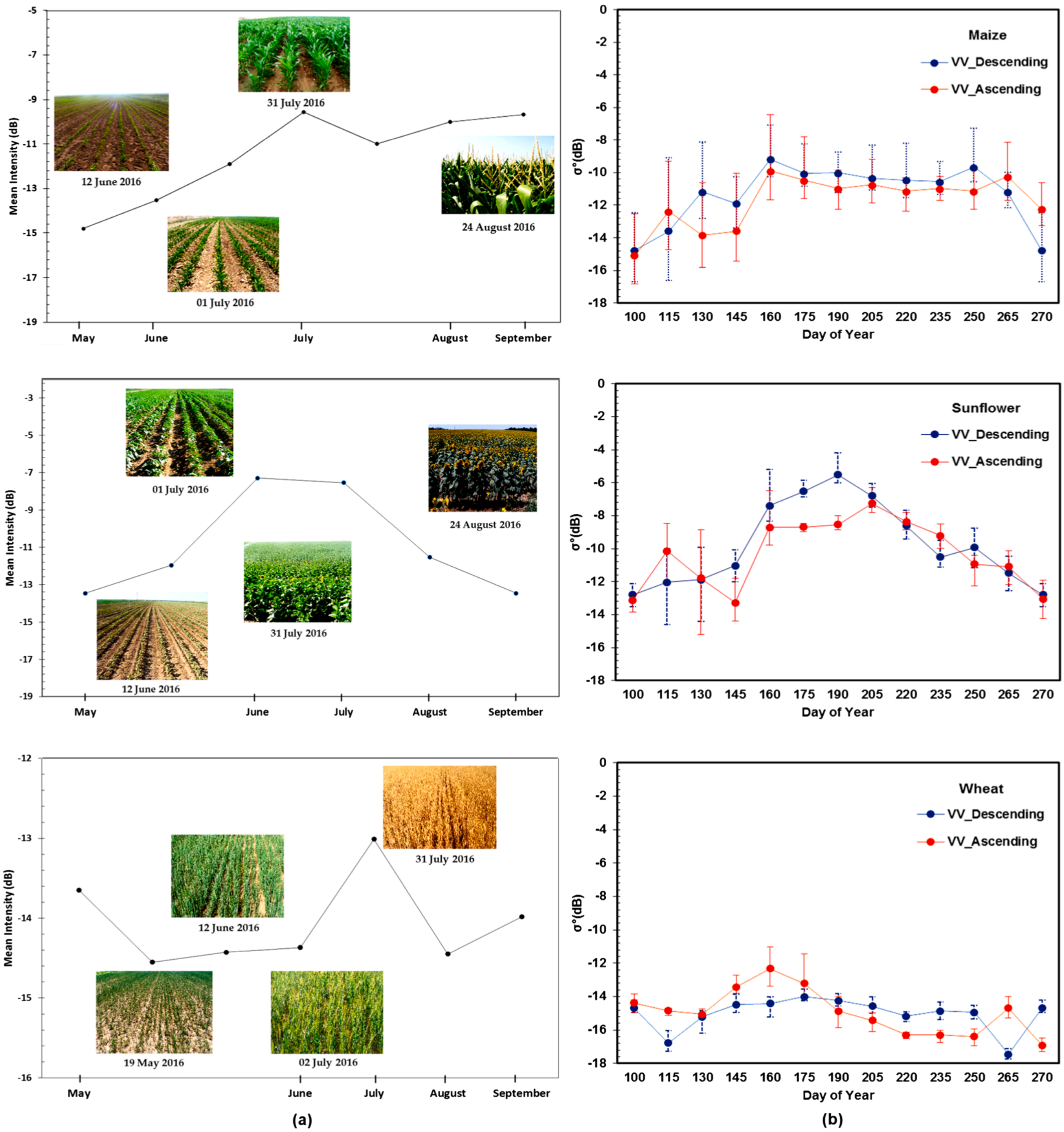

Fig. 9. Changes backscatter and development stages for a sample field **(a)**, and mean temporal backscatter profiles for all fields **(b)** for the different crop types during the growing seasons.

enabled the estimate of three main growth stages (i.e., sowing, growing, and harvesting) of the investigated crop types (maize, sunflower, wheat). Simultaneously, the multi-temporal SAR backscattering time-series analysis has provided more detailed information regarding the whole growth stages during the agricultural season and may be more profitably exploited for accurate crop assessment.

CRediT authorship contribution statement

Rouhollah Nasirzadehdizaji: Conceptualization, Methodology, Validation, Formal analysis, Investigation, Resources, Data curation, Writing - original draft, Writing - review & editing. **Ziyadin Cakir:** Conceptualization, Methodology, Validation, Investigation, Resources, Data curation, Writing - review & editing. **Fusun Balik Sanli:** Conceptualization, Methodology, Validation, Investigation, Resources, Writing - review & editing. **Saygin Abdikan:** Validation, Investigation, Resources, Writing - review & editing. **Antonio Pepe:** Validation, Investigation, Resources, Writing - review & editing. **Fabiana Calò:** Validation, Investigation, Resources, Writing - review & editing.

Declaration of Competing Interest

The authors declare that they have no known competing financial interests or personal relationships that could have appeared to influence the work reported in this paper.

Acknowledgments

The authors would like to thank Yildiz Technical University (YTU) Remote Sensing and Istanbul Technical University (ITU) National Innovation and Research Center for Geographical Information Technologies labs for providing the entire hardware and software theme required for this research.

References

Abdikan, S., Sekertekin, A., Ustunern, M., Sanli, F.B., Nasirzadehdizaji, R., 2018. Backscatter Analysis Using Multi-Temporal Sentinel-1 SAR Data for Crop Growth of Maize in Konya Basin, Turkey.

Askne, J., Santoro, M., 2003. Multitemporal repeat pass SAR interferometry of boreal forests. IEEE Trans. Geosci. Remote Sens. 43, 1219–1228. https://doi.org/10.1109/TGRS.2005.846878.

Basaran, M., 2017. Tillage-induced wind erosion in semi-arid fallow lands of Central Anatranolia. Turkey 2017, 144–151. https://doi.org/10.17221/73/2016-SWR.

Blaes, X., Defourny, P., 2003. Retrieving crop parameters based on tandem ERS 1/2 interferometric coherence images. Remote Sens. Environ. 88, 374–385. https://doi.org/10.1016/j.rse.2003.08.008.

Bron, M., Wolf, E., 2007. Principles of optics. Spectrosc. Ellipsom. 13–48. https://doi.org/10.1002/9780470060193.ch2.

Canisius, F., Shang, J., Liu, J., Huang, X., Ma, B., Jiao, X., Geng, X., Kovacs, J.M., Walters, D., 2018. Tracking crop phenological development using multi-temporal polarimetric Radarsat-2 data. Remote Sens. Environ. 210, 508–518. https://doi.org/10.1016/j.rse.2017.07.031.

Ferretti, A., Monti-guarnieri, A., Prati, C., Rocca, F., 2007. InSAR principles: guidelines for SAR interferometry processing and interpretation. ESA Publ. 1–40. https://doi.org/10.1787/9789264101630-5-en.

Just, D., Bamler, R., 1994. Phase statistics of interferograms with applications to synthetic aperture radar. Appl. Opt. 33, 4361. https://doi.org/10.1364/ao.33.004361.

Khabbazan, S., Vermunt, P., Steele-Dunne, S., Ratering Arntz, L., Marinetti, C., van der Valk, D., Iannini, L., Molijn, R., Westerdijk, K., van der Sande, C., 2019. Crop monitoring using Sentinel-1 data: a case study from The Netherlands. Remote Sensing 11 (16), 1887.

Lavreniuk, M., Kussul, N., Meretsky, M., Lukin, V., Abramov, S., & Rubel, O., 2017. Impact of SAR data filtering on crop classification accuracy. In: IEEE First Ukraine Conference on Electrical and Computer Engineering (UKRCON), pp. 912–917.

Lee, J. Sen, Grunes, M.R., Pottier, E., 2001. Quantitative comparison of classification capability: fully polarimetric versus dual and single-polarization SAR. IEEE Trans. Geosci. Remote Sens. 39, 2343–2351. https://doi.org/10.1109/36.964970.

Lopez-Sanchez, J.M., Cloude, S.R., Ballester-Berman, J.D., 2012. Rice phenology monitoring by means of SAR polarimetry at X-band. IEEE Trans. Geosci. Remote Sens. 50, 2695–2709. https://doi.org/10.1109/TGRS.2011.2176740.

Macelloni, G., Paloscia, S., Pampaloni, P., Marliani, F., Gai, M., 2001. The relationship between the backscattering coefficient and the biomass of narrow and broad leaf crops. IEEE Trans. Geosci. Remote Sens. 39, 873–884. https://doi.org/10.1109/36.917914.

Manavalan, R., 2018. Review of synthetic aperture radar frequency, polarization, and incidence angle data for mapping the inundated regions. J. Appl. Remote Sens. 12, 1. https://doi.org/10.1117/1.jrs.12.021501.

Mandal, D., Kumar, V., Ratha, D., Dey, S., Bhattacharya, A., Lopez-Sanchez, J.M., McNairn, H., Rao, Y.S., 2020. Dual polarimetric radar vegetation index for crop growth monitoring using sentinel-1 SAR data. Remote Sensing Environ. 247, 111954.

McNairn, H., Duguay, C., Brisco, B., Pultz, T.J., 2002. The effect of soil and crop residue characteristics on polarimetric radar response. Remote Sensing Environ. 80 (2), 308–320. https://doi.org/10.1016/S0034-4257(01)00312-1.

Mestre-Quereda, A., Lopez-Sanchez, J.M., Vicente-Guijalba, F., Jacob, A.W., Engdahl, M. E., 2020. Time-series of Sentinel-1 interferometric coherence and backscatter for crop-type mapping. IEEE J. Selected Topics Appl. Earth Observ. Remote Sensing 13, 4070–4084.

Nasirzadehdizaji, Rouhollah, Balik Sanli, F., Abdikan, S., Cakir, Z., Sekertekin, A., Ustuner, M., 2019. Sensitivity analysis of multi-temporal sentinel-1 SAR parameters to crop height and canopy coverage. Appl. Sci. 9, 655. https://doi.org/10.3390/app9040655.

Pepe, A., Calò, F., 2017. A review of interferometric synthetic aperture RADAR (InSAR) multi-track approaches for the retrieval of Earth's Surface displacements. Appl. Sci. 7, 1–40. https://doi.org/10.3390/app7121264.

Perissin, D., Wang, T., 2012. Repeat-pass SAR interferometry with partially coherent targets. IEEE Trans. Geosci. Remote Sens. 50, 271–280. https://doi.org/10.1109/TGRS.2011.2160644.

Rosen, P.A., Hensley, S., Zebker, H.A., Webb, F.H., Fielding, E.J., 1996. Surface deformation and coherence measurements of Kilauea Volcano, Hawaii, from SIR-C radar interferometry Abstract. The shuttle imaging radar C/X synthetic radar on board the space Endeavor for the purpose of measuring active surface deformation by. J. Geophys. Res. 101, 109–125.

Saich, P., Borgeaud, M., 2000. Interpreting ERS SAR signatures of agricultural crops in Flevoland, 1993–1996. IEEE Trans. Geosci. Remote Sens. 38, 651–657. https://doi.org/10.1109/36.841995.

Sandwell, D., Mellors, R., Tong, X., Wei, M., Wessel, P., 2011. Open radar interferometry software for mapping surface deformation. Eos Trans. AGU 92 (28). https://doi.org/10.1029/2011EO280002.

SNAP - ESA Sentinel Application Platform v6.0.7, http://step.esa.int.

Stankiewicz, K.A., 2006. The Efficiency of Crop Recognition on ENVISAT ASAR Images in Two Growing Seasons 44, 806–814.

Steele-dunne, S.C., Mcnairn, H., Monsivais-huertero, A., Judge, I.J., 2017. Radar Remote Sensing of Agricultural Canopies: A Review https://doi.org/10.1109/JSTARS.2016.2639043.

Tamm, T., Zalite, K., Voormansik, K., Talgre, L., 2016. Relating Sentinel-1 interferometric coherence to mowing events on grasslands. Remote Sens. 8, 1–19. https://doi.org/10.3390/rs8100802.

Ulaby, F.T., 1981. Microwave Remote Sensing Active and Passive I, 1–48.

Veloso, A., Mermoz, S., Bouvet, A., Le Toan, T., Planells, M., Dejoux, J.F., Ceschia, E., 2017. Understanding the temporal behavior of crops using Sentinel-1 and Sentinel-2-like data for agricultural applications. Remote Sensing Environ. 199, 415–426.

Vreugdenhil, M., Wagner, W., Bauer-Marschallinger, B., Pfeil, I., Teubner, I., Rüdiger, C., Strauss, P., 2018. Sensitivity of Sentinel-1 backscatter to vegetation dynamics: an Austrian case study. Remote Sensing 10 (9), 1396.

Wegmüller, U., Werner, C., 1997. Retrieval of vegetation parameters with SAR interferometry. IEEE Trans. Geosci. Remote Sens. 35, 18–24. https://doi.org/10.1109/36.551930.

Wooding, M.G., Attema, E., Aschbacher, J., Borgeaud, M., Cordey, R.A., Groof, D.H., 1995. Satellite radar in Agriculture - Experience with ERS-1, SP-1185 Noordwijk, The Netherlands: European Space Agency. Worbes, M.

Zalite, K., Voormansik, K., Praks, J., Antropov, O., Noorma, M., 2014. Towards detecting mowing of agricultural grasslands from multi-temporal COSMO-SkyMed data. In: Int. Geosci. Remote Sens. Symp., pp. 5076–5079. https://doi.org/10.1109/IGARSS.2014.6947638.

Zebker, H.A., Villasenor, J., 1992. Decorrelation in interferometric radar echoes. IEEE Trans. Geosci. Remote Sens. 30 (5), 950–959.

Zhou, T., Pan, J., Zhang, P., Wei, S., Han, T., 2017. Mapping winter wheat with multi-temporal SAR and optical images in an urban agricultural region. Sensors (Switzerland) 17, 1–16. https://doi.org/10.3390/s17061210.